Correlation between the microstructure and corrosion performance of the HIPIMS nitrided bio-grade CoCrMo alloy

SHUKLA, Krishnanand, PURANDARE, Yashodhan <http://orcid.org/0000-0002-7544-9027>, SUGUMARAN, Arunprabhu, EHIASARIAN, Arutiun <http://orcid.org/0000-0001-6080-3946>, KHAN, Imran and HOVSEPIAN, Papken <http://orcid.org/0000-0002-1047-0407>

Correlation between the microstructure and corrosion performance of the HIPIMS nitrided bio-grade CoCrMo alloy.

Krishnanand Shukla[1*], Yashodhan Purandare[1], Arunprabhu Sugumaran[1], Arutiun Ehiasarian[1], Imran Khan[2] and Papken Hovsepian[1]

[1]National HIPIMS Technology Centre UK, Materials and Engineering Research Institute, Sheffield Hallam University, Sheffield, S1 1WB, UK.

[2]Zimmer-Biomet UK Limited, Dorcan Industrial Estate, Murdock Road, Swindon SN3 5HY, UK.

*** Corresponding author: krishnanand.shukla@student.shu.ac.uk**

Abstract:

Corrosion performance of CoCrMo alloy (F75) plasma nitrided with High-Power Impulse Magnetron Sputtering (HIPIMS) technique was thoroughly investigated. Open Circuit Potential (OCP) measurements and potentiodynamic polarisation tests exhibited a strong correlation between the transmuting microstructure (as a result of varying nitriding voltage from -700 V to -1100 V) and its corrosion performance. A significant improvement in the E_{Corr} values was noticed (around -590 mV for untreated as compared to -158.17 mV for -1000 V) when analysed against 3.5% wt. NaCl solution. Similarly, results against Hank's solution also exhibited a significant increase in E_{Corr} values (around -776 mV for untreated as compared to -259 mV for -1000 mV). Irrespective of the nitriding voltage, HIPIMS nitriding led to a significant improvement in the corrosion resistance of the alloy. For nitriding voltages -700 V and -900 V, a diffusion based S phase layer played a significant role in imparting corrosion resistance. On the

contrary, precipitation of chromium-based nitrides (CrN and Cr_2N), observed in samples nitrided at relatively higher voltages of -1000 V and -1100 V, resulted in its relative deterioration. A preferential dissolution of the ϵ_N grains and its grain boundaries, along with a sluggish dissolution of the γ_N grains and metal carbides appeared to be the dominant corrosion mechanism for the nitrided alloys. Specimens nitrided at -700 V and -900 V displayed the best corrosion resistance, which was deemed to be derived from the right combination of a thicker S phase layer and the compound layer consisting of $M_{2\text{-}3}N$ and M_4N phases.

Keywords: Hip joints; CoCrMo alloy; HIPIMS nitriding; simulated body fluid; corrosion.

1. Introduction.

High and Low-carbon CoCrMo (F75/F1537) alloys remain a popular choice for the development of total joint replacements (artificial) such as Hip/Knee prosthetics owing to its good corrosion resistance, biocompatibility and superior mechanical properties in the physiological environment [1], [2], [3], [4]. However, wear of this material due to friction in the long run, is still a major concern for researchers as it can damage the articulating surfaces and the surrounding cartilage [5][6]. Along with this, the release of metal ions in the presence of larger debris (50-120 nm) [7] can induce numerous adverse health effects [8], [9].

Besides mechanical integrity, corrosion resistance of the alloy is also critical and a lack of it can have an antagonistic effect on the mechanical properties and biocompatibility. The main source of extra ions in the body is the dissolution of surface oxides and corrosion of the material,[8], [10], [11]. In order to avoid any toxic reaction on the human body, the implant material should retain its functional properties and corrosion resistance at the same time. Considerable amount of ion release from the implanted material can lead to serious illness due to biological reactions. For example, research shows that the presence of excessive amount of Cr (VI) in the human body can change the reproductive behaviour, and can increase the chances of cellular toxicity [12]. On the other hand, excess amount of Co ions in human body can also increase the chances of thyroid which may increase the chances of asthma, overproduction of erythrocytes and fibrosis in lungs [13], [14]. It is now well known that biocompatibility of an alloy is related to its corrosion resistance and its ability to passivate. In the case of CoCrMo alloy, formation of mostly Cr_2O_3 passive layer with some contribution from Co and Mo based oxides has been widely reported [15], [16], [17], [18], [19], [20], [21].

To minimise the wear rate of the implant material (here CoCrMo alloy) various state of the art methods have been applied including surface alloying technique [1], [3], [22], [23] coatings such as TiN, CrN and NbN, [24], [25], nanoscale multilayer coatings, [26], [27] and duplex coatings, [28]. Literature on plasma nitriding of biomaterials such as Ti alloys and stainless steel suggests that nitriding leads to a significant reduction in wear rate and friction coefficient of these alloys as compared to the untreated alloys, [29], [30], [31]. There is also a clear consensus that nitriding of CoCrMo alloys improves its hardness and consequently its wear resistance. Plasma-assisted alloying has been promising in that aspect. It has proven to be an effective and reliable solution, wherein formation of a thick compound layer consisting of $Co_{2\text{-}3}N$+Cr_4N phases was found to improve mechanical properties, and wear resistance significantly [32]. However, there is a lack of consensus on the corrosion resistance offered by the nitrided surfaces irrespective of the base alloy (Ti, Fe as well as CoCrMo alloys) owing to the severe lack of literature. Sparsely available reports suggest that corrosion resistance of nitrided surfaces is highly influenced by its structural and phase composition. For example, in the case of CoCr based alloys, both, an improvement [33], [34] as well as deterioration in corrosion resistance [3], [35] due to nitriding has been reported. On the contrary, further enhancement in corrosion resistance due to the precipitation of Cr based nitrides (CrN and Cr_2N) in the nitrided layer has also been reported [34]. Corrosion tests results has also shown a dependency on the chemical composition of the test solution used (different Simulated Body Fluids (SBFs), bovine serum, different NaCl concentrations, etc.) [36], [37], [16] and that the test results cannot be simply carried over across different corrosive mediums. It is evident that more work is necessary to understand this complex phenomenon.

Earlier work on nitriding of CoCrMo alloy utilising the novel High Power Impulse Magnetron Sputtering (HIPIMS) discharge showed that this technique can be successfully applied to

improve the wear resistance of the base alloy [1], [32], [38]. These works showed that the choice of nitriding voltage determines the phase composition and microstructure of the nitrided layer and hence the mechanical properties of these engineered surfaces [1]. However, the effect of the metallurgy and the microstructure of these modified layers on the corrosion resistance had yet to be explored.

This work aims to thoroughly investigate the corrosion performance of the CoCrMo alloys nitrided at different nitriding voltages with the HIPIMS technique. The effect of nitrided layer composition on the corrosion resistance of the CoCrMo alloy has been investigated in both 3.5 wt% NaCl solution (widely available literature on corrosion on corrosion of metals and alloys, hence facilitates an easy comparison) and a SBF-Hank's solution. Three cell electrode electrochemistry and scanning electron microscopy has been utilised thoroughly to investigate the relation between microstructure and the corrosion performance of the nitrided specimen. These results provide further insight to clear the existing ambiguity on the corrosion resistance offered by nitrided CoCrMo alloys.

2. Experimental Method

2.1 Plasma Nitriding utilising HIPIMS discharge:

Disc-shaped specimens of 26 mm diameter (φ) and 6 mm thickness (d) made from CoCrMo alloy (ASTM F75, Zimmer-Biomet, UK) were prepared to a mirror-like surface finish (R_a= 13 nm) by using a standard metallographic procedure. The chemical composition of the CoCrMo alloy (F75) alloy is presented elsewhere, [1]. Before the nitriding procedure, the specimens were cleaned using an automated industrial cleaning line consisting of several ultrasonic baths containing different alkali solutions, rinsing with deionised water followed by vacuum drying. After cleaning, the specimens were immediately loaded into the vacuum chamber (industrial

sized PVD coating machine-Hauzer techno Coating 1000-4, The Netherlands empowered by HIPIMS technology at Sheffield Hallam University, UK). Prior to the nitriding process, the surface of the specimens was pretreated to remove remaining surface contaminants (oxides) by metal ion etching [39], [40]. At this stage of the process, the surface was subjected to an intensive bombardment of metal ions (Cr^+) produced by HIPIMS discharge sustained on one Cr target (99.9 % pure) operated with a HIPIMS power supply (Hüttinger Elektronik Sp. z o.o., Warsaw, Poland), [41]. The nitriding voltage was applied with the help of a dedicated bias power supply (Hüttinger Elektronik Sp. z o.o., Warsaw, Poland), [42]. Four different nitriding voltages were employed; namely -700V, -900 V, -1000 V and -1100 V which represent 4 different conditions of the ionic energies (flux) incident on the specimens. Details of the nitriding process can be found in the previous publication [1].

2.2 Characterisation Techniques:

1. Thickness, microstructure of the compound layer of the nitrided CoCrMo alloy and the corroded surfaces were investigated using cross sectional (CS-SEM) and plan view scanning electron microscopy (*FEI Quanta 650 3D DualBeam FIB FEG-SEM*) equipped with both secondary and backscattered detectors and an Energy Dispersive X-Ray Spectroscopy (EDS) system. For cross-section SEM analysis, small sections from the nitrided samples were cut, metallurgically mounted and polished. Following polishing, the surfaces were chemically etched using a mixture of hydrogen peroxide (H_2O_2) and hydrochloric acid (HCl) (Marble's reagent) for 15-25 seconds and washed with de-ionised water. For imaging corroded surfaces, the samples were rinsed with de-ionised water and dried with a handheld dryer after the experimentation before imaging. An Olympus (BX51M) optical microscope was used to capture optical images of the surfaces

wherever appropriate. X-ray diffraction (XRD) studied were performed on an Empyrean X-ray diffractometer using Cu Kα radiation (1.5418 Å) using a glancing angle (2° incidence) technique (2θ, 20-100° (step size = 0.026 (°2θ), step time = 198.64 s)).

2. Potentiodynamic polarisation tests were performed to analyse the corrosion performance of the nitrided and untreated specimens in 3.5 wt% NaCl solution using a computer-controlled *Gill-AC* potentiostat. The test set-up formed a 3-electrode corrosion cell with the specimen as the working electrode, carbon rods as auxiliary electrode and a saturated Silver/Silver chloride electrode (Ag/AgCl) as the reference electrode. The tests specimens were masked with a non-conductive lacquer to expose 1 cm^2 of the specimen (area of interest) to the corrosive solution. The specimens were catholically cleaned at -1500 mV. After immersion in the aerated solution for 20 mins, Open Circuit Potentials (OCP) were recorded for 40 mins. Following OCP measurements, the test specimens were polarised from -1000 mV to +1000 mV with the scan rate of 1 mVs^{-1}. All electrochemical potentials reported in this article are with respect to the Ag/AgCl reference electrode. Every experiment was repeated twice to examine repeatability of the results.
3. To predict the corrosion behaviour of the specimens in a biological environment (human body environment), testes were also repeated in a SBF (Hank's solution). The measured pH value of the solution was in the range of 7.1-7.3. All the tests were performed at room temperature conditions and the temperature of the solution was in the range of 27°-30° C.
4. Corrosion products formed on the surfaces were analysed using a Raman spectrometer (*LabRam HR800, Horiba-Jobin-Yvon, France*) fitted with a green laser (λ = 532 nm, 5 mW output power). To collect the spectra, 100 % power was used. Before the analysis,

corroded surfaces were rinsed with de-ionised water followed by hot air drying. The Raman spectra were collected using computer software (*Lab-Spec version 5*) embedded with spectrometer. Later, data was further processed using *Origin 9.0* data analysis software.

3 Results and Discussion

3.1 Microstructure and Cross-Section Analysis:

Fig.1a shows the SEM image of the untreated CoCrMo (F75) alloy microstructure. The structure consists of a metastable f.c.c austenite (γ) and h.c.p (ε) phase matrix with a random distribution of metal carbide dendrites, which is consistent as reported earlier [43], [44]. In order to understand the metal carbide composition in depth, EDS analysis of the untreated alloy was performed. Results showed that the carbide phases consisted of a mixture of metals (Co, Cr, Mo and Mn) of around 66.7 at% with a carbon concentration of around 33.3 at %. Figure 1b shows the carbide phase at high magnification (indicated by a square inset in figure 1a) and the chemical composition of the carbide phase (inset table).

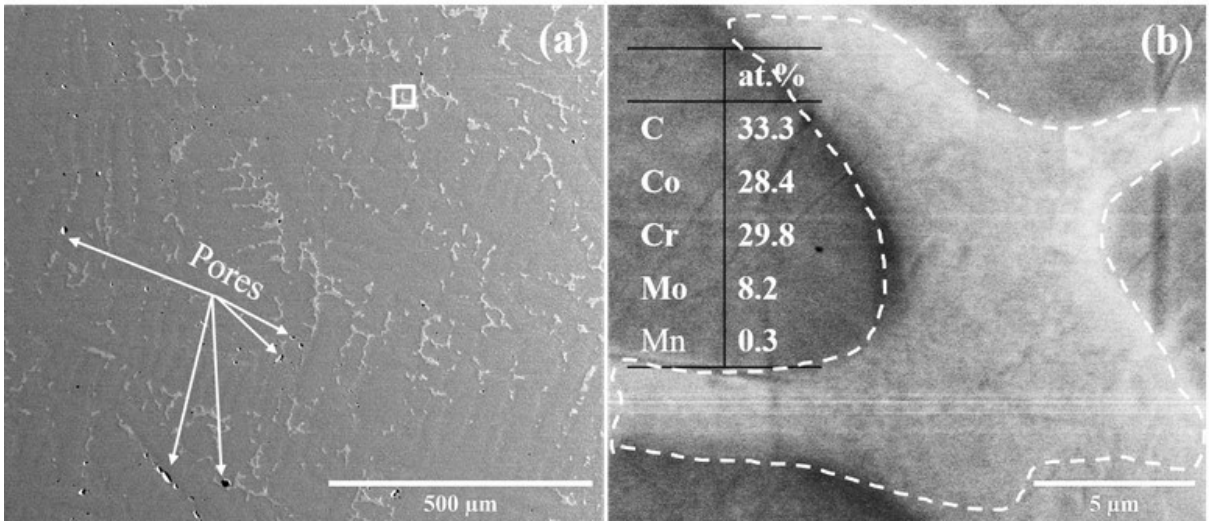

Figure 1: (a) Low magnification image of the microstructure of CoCrMo (F75) alloy in plan view. (b) Area indicated by square inset of 1a at high magnification showing the carbide phase and the results obtained from the compositional EDS analyses.

The metal carbides can be found in different shapes and sizes depending on the crystal structure of the phase. These finely distributed carbides can be identified as $M_{23}C_6$, however the size, transformation (into M_6C) and distribution of this phase can vary based on the manufacturing process and the composition [45], [46]. As exhibited in figure 1 (a), the carbide phases in the microstructure of the alloy used in this study had irregular shapes and sizes. Moreover, they had a dense and blocky appearance which is typical for $M_{23}C_6$ type of metal carbide [45]. Apart from the carbides, porosity (indicated by the arrows in figure 1a) resultant due to the breaking of brittle carbide phases during polishing could also be observed.

Figure 2 (a-d) shows the microstructures of the specimens nitrided at different voltages in a plan view. As observed in figure 2(a-b) and the XRD results in 2(e) the microstructure of the nitrided layers (-700 and -900 V specimens) consisted of a mix of equiaxed grains of γ_N phase, and randomly distributed carbides (mainly $M_{23}C_6$ phases) within the γ_N phase. Presence of equiaxed

grains of the ϵ_N phase could also be speculated considering the evidence from the current xrd results. Interestingly, γ_N phase dominated the microstructure in the case of the two specimens nitrided at lower voltages.

Microstructure of the specimens treated at higher nitriding voltages (-1000 V, and -1100 V), figure 2(c-d), also exhibited equiaxed grains of γ_N phase along with the random distribution of $M_{23}C_6$ carbides. However, a striking difference in the microstructure for these specimens was the presence of possible ε plates and possibly of deformation twins within the γ_N phase grains (inset image of figure 2c). In this case, deformation twins were visible at high magnification with the distance between two lines in the range of 60-80 nm. No deformation twins were visible in the case of -1100 V. With the available SEM and xrd results (figure 2) it could be speculated that higher nitriding voltages (>1000 V and -1100 V in this case) promoted the formation of ϵ_N phase, which makes the surface much harder. Earlier work on HIPIMS plasma nitriding on CoCrMo alloy [1] showed that the texture of these nitrided specimens changed from a predominant (200) orientation (-900 V nitrided specimen) to a mixture of (111) + (200) orientations (-1100V nitrided specimen).

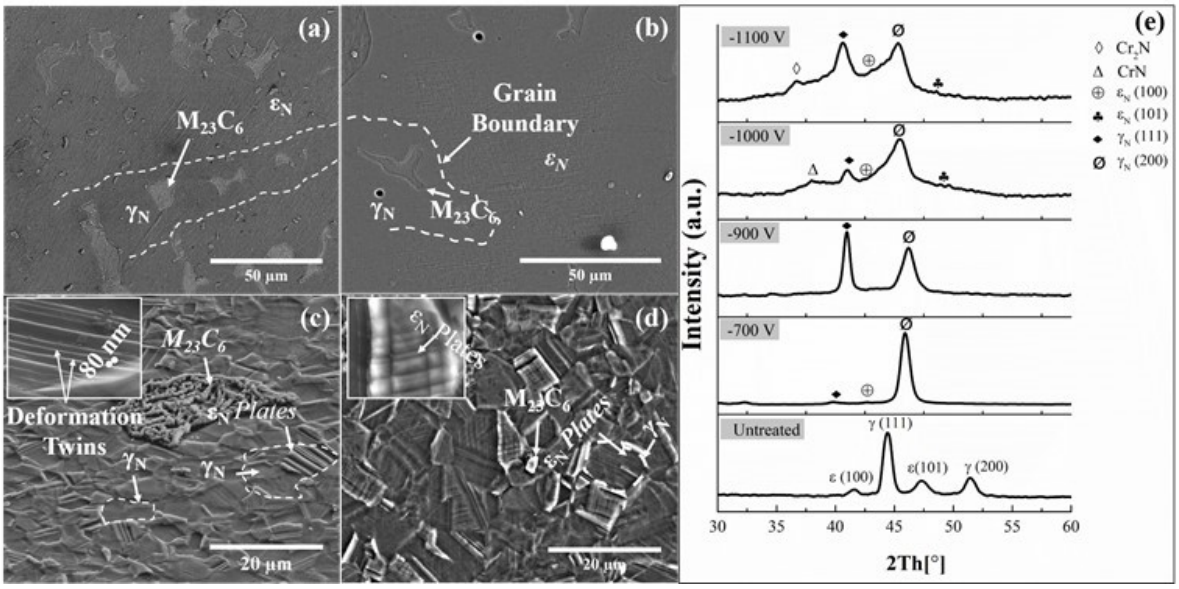

Figure 2: SEM microstructure of plasma nitrided CoCrMo alloy at (a) -700 V (b) -900 V (c)-1000 V and (d) -1100 V. Inset images in (c) and (d) show a selected area at a higher magnification with (possibly) deformation twins and ε_N plates respectively (e) XRD results showing the presence of different phases in the untreated and the treated alloys (reproduced from reference [1]).

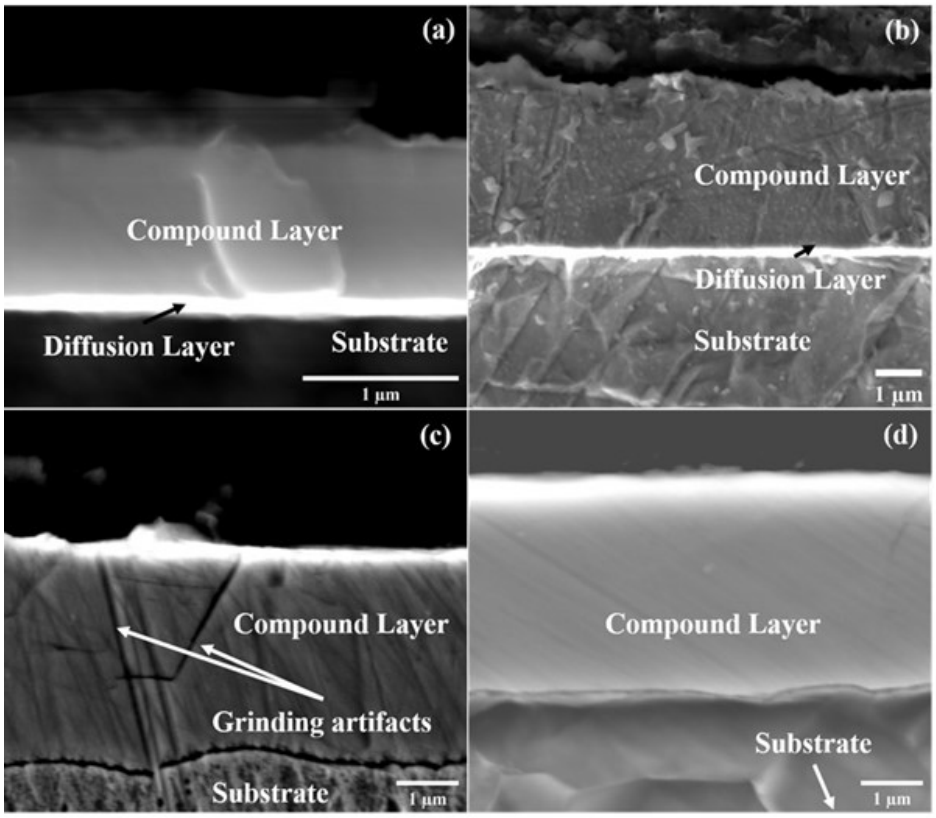

Figure 3: Cross-sectional micrograph of the specimens nitrided at (a) -700 V (b) -900 V (c) -1000 V and (d) -1100 V showing the grey compound layer ($Co_{2-3}N$+Co_4N) and the light contrast diffusion layer (Co_4N). Specimens were etched for 20 seconds with Marble's reagent (H_2O_2+HCL).

Figure 3 presents the cross-sectional view of these plasma nitrided specimens. Specimens nitrided at -700 V and -900 V clearly revealed the formation of two distinct layers; namely a diffusion layer- Co_4N (also defined as a S phase layer [3], [33], [47]) which appeared as a bright layer at the substrate interface and a compound layer ($M_{2-3}N$ and M_4N, where M= was mainly Co dominated)) which appeared as a grey colour layer on top of the diffusion layer [1]. The thickness of the diffusion layer increased with the increase in nitriding voltage from 130 nm (-700 V) to 283 nm (-900 V), Fig. 3a and b respectively. The diffusion layer was not clearly

visible for specimen nitrided at higher voltages of -1000 V and -1100 V and the cross-sectional imaging only revealed the thick compound layers formed on the top of the substrate (Fig. 3c and d respectively). XRD studies (figure 2(e)) also suggested the precipitation of CrN and Cr_2N phases for these high voltage nitrided specimens; details of which have been presented elsewhere [1]. It can be speculated that, even though not visible, the conditions of nitriding may have promoted a limited formation of the diffusion-based S phase layer at the substrate interface and beneath the build-up of the thick compound layer.

In general, an increase in the nitriding voltage led to an increase in the overall thickness of the nitrided layer. The total nitrided layer thickness (diffusion layer + compound layer) measured were 1.28 ± 0.05 μm for -700 V, 2.83 ± 0.12 μm for -900 V, 3.68 ± 0.19 μm for -1000 V and 4.77 ± 0.19 μm for -1100 V. This increment in thickness could be attributed to the augmentation of ion energies with more negative voltages which are incident on the substrate and also to the associated increase in the surface temperature [1] which lead to the increment of the diffusion rate of N [1], [34], [45], [49]. Irrespective of the applied voltage, the nitrided layers appeared uniform in thickness, dense in nature and defect free (any plasma process related defects such as contamination from the chamber walls) which also resulted, in general, in a smoother surface finish of the specimens.

3.2 Corrosion Studies:

3.2.1 Electrochemical studies in 3.5 wt% NaCl solution

Figure 4a displays the evolution of OCP as a function of time. All the nitrided specimens exhibited a rapid increase in the potential values before reaching near-steady state values. The

untreated CoCrMo alloy had the lowest rate of increase, which suggested a gradual passivation of the surface. The specimen nitrided at -900 V had the noblest OCP value followed by specimen nitrided at -700 V and -1000 V. Barring the -1100 V specimen, which exhibited a gradual drop in the curve after attaining a peak (around 750 seconds of recording), all the nitrided specimens performed better as compared to the untreated alloy. Smooth, unfluctuating, and continuous nature of the OCP curves suggests that the nitrided layers were homogenous, defect free and continuous in structure indicating a superior quality.

The potentiodynamic polarisation curves of the untreated and nitrided specimens are shown in figure 4b. Corrosion current densities (I_{Corr}, $mAcm^{-2}$) and corrosion potentials (E_{Corr}, mV) were extracted from the polarisation curves using standard Tafel analysis (using the Sequencer software-ACM instruments) and values are presented in Table 1. As evident, all the specimens showed a clear difference in terms of E_{Corr} values, anodic dissolution, passivation and transpassivation domains and the significance of nitriding voltage and consequential microstructure in determining them was enormous. Amongst these, the shift in E_{Corr} values was noticeable. It is evident that, irrespective of the nitriding voltage, the improvement in corrosion resistance of the base CoCrMo alloy was significant. In comparison, the untreated CoCrMo alloy exhibited a clear and a stable passivation domain in the potential ranges of -380 mV to +100 mV. This passive behaviour has been attributed to the formation of Cr based oxides films (mainly to the formation of Cr_2O_3/Cr $(OH)_3$))formed in air which are difficult to remove [50], [51]. Beyond +200 mV formation of Cr (VI) species in the passive layers, increasing fraction of CoO and Mo, dissolution of Co at higher anodic potentials, significant increase in the passive layer thickness and dissolution of these passive films along with the water oxidation reactions led to the rapid rise in the current values [34], [37], [48], [52]. Despite a limited but a clear and stable

passive domain, the bare alloy exhibited higher anodic currents and had the lowest E_{Corr} value (-527 mV) among the samples analysed thus implied a poor corrosion resistance.

The sample nitrided with -900 V showed a significant upward shift to exhibit the most noble E_{Corr} value (-126 mV). The corrosion kinetics of this sample could be described as follows. After a brief passivation in the -150 mV to 60 mV polarisation interval, the polarisation curve indicated a high dissolution rate in the 60 mV to 260 mV interval, followed by the tendency of re-passivation in the potential range of around +250 mV to +460 mV. The microstructure of this specimen, figure 3b, predominately consisted of a distinct, uniform S phase band at the interface of the base alloy and a compound layer consisting of both $M_{2\text{-}3}N$ and M_4N (where M is mostly Co dominated). Several reports on nitriding of CoCrMo or Fe based alloys in the literature have attributed the improvement of corrosion resistance to the presence of the S phase structure [33], [35], [47]. On the other hand, structures dominated by Co based compounds have shown a poor corrosion performance due to the ready dissolution of the Co from these compounds [52]. Thus, consistent with the literature, the corrosion behaviour of the -900 V nitrided specimen seemed to be a weighted mixture of the corrosion performances of the two microstructures; namely the S phase and the Co based compounds. Improvement in the E_{Corr} value and lower corrosion currents in the anodic ranges unto +60 mV could be attributed to the presence of a distinct but a homogenous S phase diffusion layer. The smaller repassivation attempt of the specimen above +250 mV (potentials between +250 mV and +460 mV) could be attributed to the passivation of Cr (either from the base alloy or dispersed Cr present in the nitrided layer). Beyond potentials of around + 460 mV, the polarisation curve was dominated by the dissolution of both Co and Cr [50].

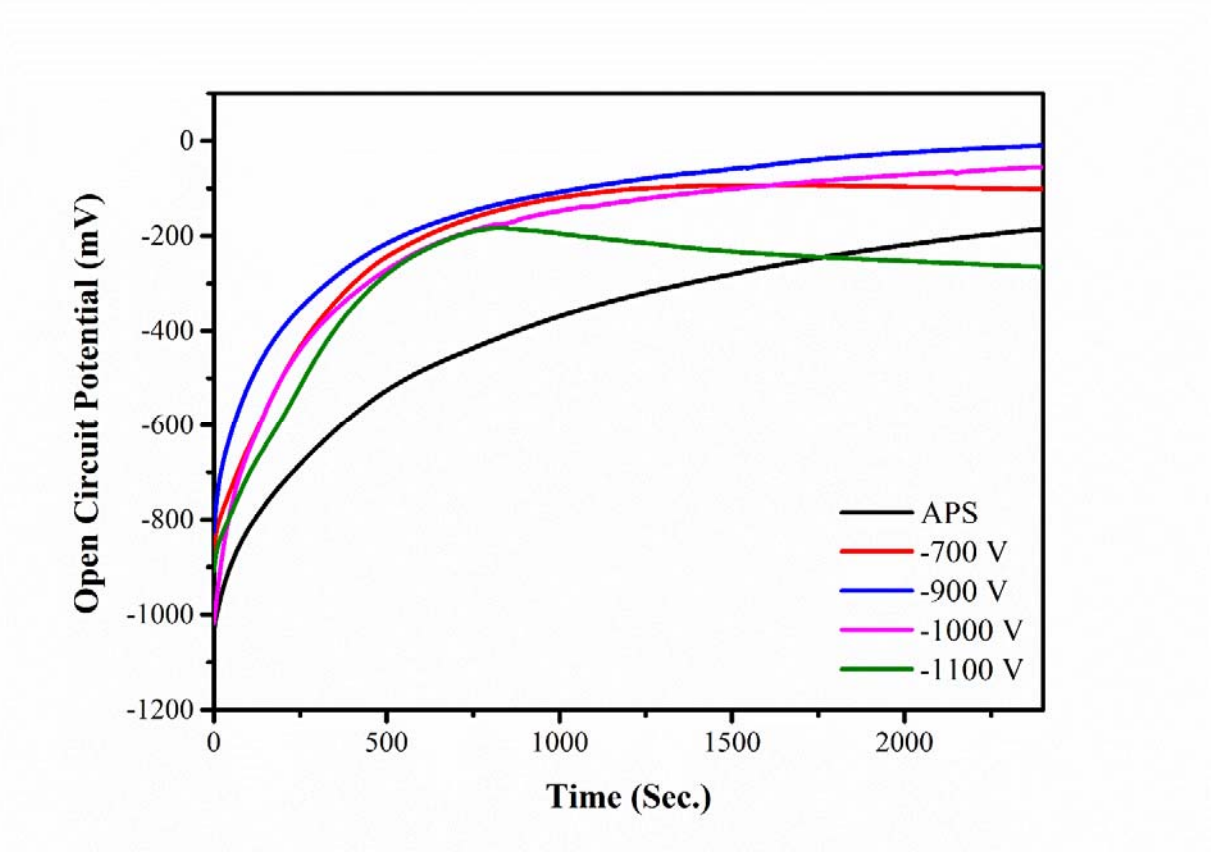
Open Circuit Potential (mV)
0
-200
-400
-600
-800
-1000
-1200
0
500
1000
1500
2000
Time (Sec.)
APS
-700 V
-900 V
-1000 V
-1100 V

(a)

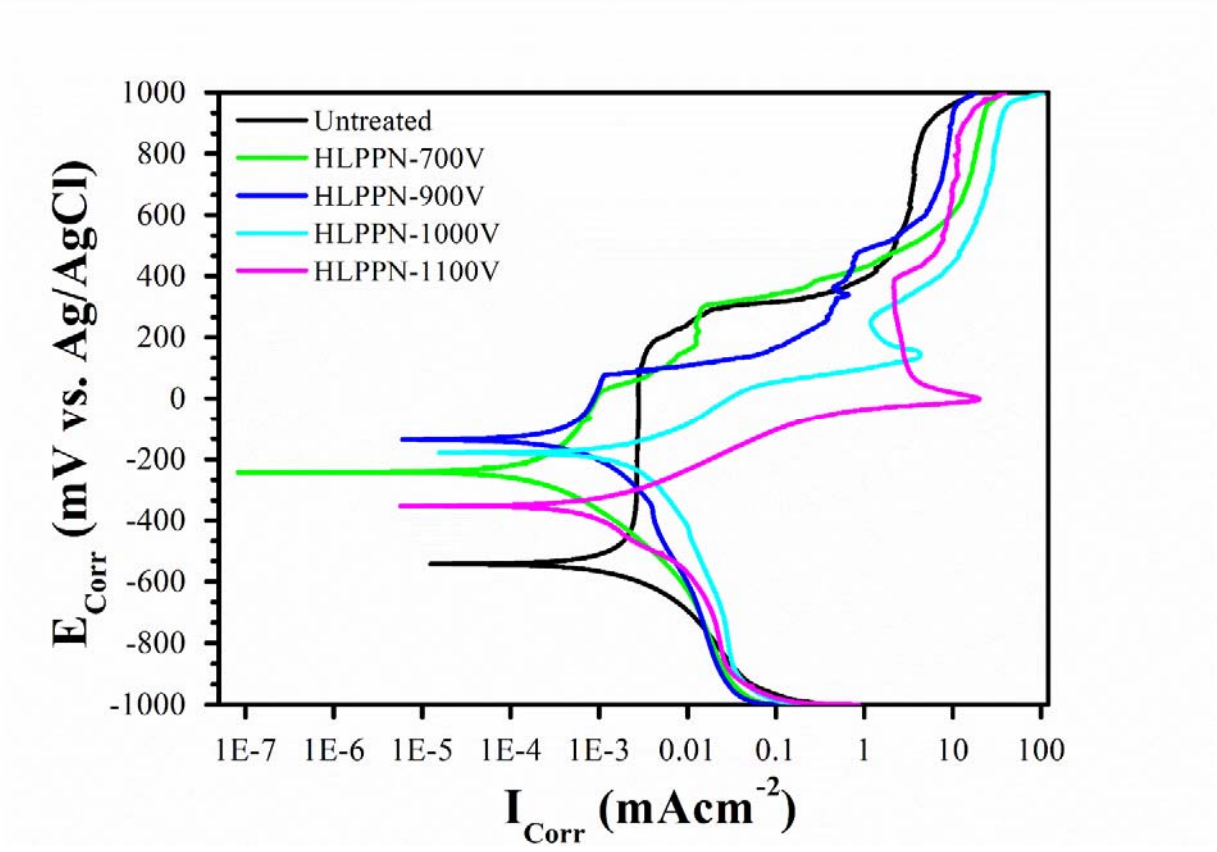

(b)

Figure 4: (a) Open circuit potential (OCP) and (b) Potentiodynamic polarisation curves of the untreated specimen and specimens nitrided at various bias voltage (-700 V to -1100 V) submerged in 3.5 wt.% NaCl solution.

The specimen nitrided at -700 V nearly mimicked the corrosion performance of the -900 V, except for a slight drop in the E_{Corr} value (-242 mV) and the repassivation potentials (a drop in value from +250 mV to around +180 mV). The microstructure of this specimen, figure 3a, essentially, also resembled to -900 V, albeit a thinner compound layer and a slimmer diffusion

band consisting of the S phase structure. Thus, the reduction in E_{Corr} value of -700 mV sample was consistent with the microstructural changes.

In the case of -1000V and -1100 V specimens, figure 3 (c-d), the microstructures were made up of relatively thicker compound layers which consisted of a mixture of both $M_{2-3}N$ and M_4N compounds and were also estimated to have a thin S phase diffusion band at the interface between nitrided layer and the base alloy. XRD results [figure 2(e)] also showed peaks pertaining to precipitation of CrN (-1000 V) and Cr_2N (-1100 V) phases as a result of temperature rise leading to a localised heating (for e.g., temperatures reached 520 °C in the case of nitriding with -1100 V) due to the intense bombardment of the ions. Despite having thicker compound layers, the corrosion performance of -1000 V and -1100 V specimens, in general, was inferior compared to -700 V and -900 V specimens. The E_{Corr} value of -1000 V specimen (-158.17 mV) and -1100 (-351.33 mV) was lower to -700 V (-126.28 mV) and -900 V (-133.39 mV) specimens, but higher than the untreated base alloy (-590.63 mV). The anodic domains of these were identical as far the shape is concerned and showed a high dissolution (one of the highest I_{Corr} values in this study), with no tendency to passivate until potentials of around +140 mV for -1000 V specimen and around +20 mV for -1100 V specimen. The clear difference in performance between the -1100 V specimen and other specimens is the observation of a broader passive domain, albeit higher corrosion currents, between potentials +20 mV and +370 mV and could be attributed to the limited passivation, in this case, offered by the thinner S phase layers and to some extent by the Cr precipitates [50], [53]. The disadvantages of Cr precipitates in the nitrided microstructure was consistent with those reported earlier [21], [52].

Thus, in this study, when analysed against 3.5 % NaCl, the corrosion performance of the nitrided specimens showed a strong dependency on the microstructure. A clear passivating behaviour of

the untreated CoCrMo alloy (because of the readily available Cr from the metal matrix composite) was lost to the nitriding process. However, this loss appeared to be compensated by the S phase structure and the metal nitrides (mostly Co) obtained by nitriding; evident in terms of higher E_{Corr} values and lower I_{Corr} values in most anodic domains for -700 V and -900 V nitrided specimens.

Electrolyte	**3.5 wt.% NaCl**					
Repetition	**SET-1**			**SET-2**		
Sample ID	**E_{Corr} (mV)**	**I_{Corr} ($mAcm^{-2}$)**	**OCP (mV)**	**E_{Corr} (mV)**	**I_{Corr} ($mAcm^{-2}$)**	**OCP (mV)**
Untreated	-590.63	$8.50E^{-5}$	-186.29	-601.03	$8.68E^{-06}$	-188.57
-700 V	-242.24	$1.35E^{-4}$	-13.33	-237.56	$1.51E^{-05}$	-31.31
-900 V	-133.39	$6.06E^{-5}$	-96.46	-178.52	$4.71E^{-05}$	-57.21
-1000 V	-158.17	$9.19E^{-5}$	-153.65	-177.46	$2.60E^{-04}$	-171.77
-1100 V	-351.33	$2.21E^{-4}$	-257.86	-334.76	$1.11E^{-04}$	-259.97

Table 1: Corrosion analysis data obtained from the polarisation curves of the nitrided specimens and the untreated specimen when analysed against 3.5 wt% NaCl.

3.2.2 Electrochemical Studies in SBF (Hank's Solution)

CoCrMo alloy has been widely used in medical implant applications such as hip replacement (metal-on-metal). The body environment is considered to be very complex and contains various salts, amino acids, lipids and proteins [54]. Once the implant submerges in the body fluids such as saliva and buffer solution, the behaviour of the material exceedingly changes due to corrosion process [16], [19], [55]. Hence, analysis of the untreated and nitrided specimens for its corrosion

behaviour in SBF was deemed essential. In this study, Hank's solution was chosen as the SBF and the composition of Hank's solution is presented in table2.

Inorganic Salts	Concentration (mg/L)	Amino Acids	Concentration (mg/L)
$CaCl_2$-$2H_2O$	185	L-Arginine hydrochloride	126
$MgCl_2$-$6H_2O$	100	L-Cystine	21
$MgSO_4$-$7H_2O$	100	L-Glutamine	292
KCl	400	L-Histidine hydrochloride-H2O	42
KH_2PO_4	60	L-Isoleucine	52
$NaHCO_3$	350	L-Leucine	52
NaCl	8000	L-Lysine hydrochloride	73
Na_2HPO_4	48	L-Methionine	15
Glucose-D	1000	L-Phenylalanine	32
		L-Threonine	48
		L-Tryptophan	10
		L-Tyrosine	36

Table 2: Composition of Simulated body fluid (Hank's Solution).

Figure 5a shows the OCP curves recorded as a function of time. Similar to the NaCl results, all the nitrided specimens exhibited a rapid increase in the potential values with time before reaching near-steady state values. However, in the case of the untreated alloy, the potential rose gradually to a near-steady state suggesting that passive layer formation was less effective in

retarding the corrosion currents as compared to the nitrided specimens. A clear hierarchy in the OCP values was observed where the specimen nitrided at -900 V had the noblest OCP value followed by those nitrided at -700 V, -1000 V and -1100 V respectively. Table 3 provides the corrosion parameters such as I_{Corr} (corrosion current density, mAcm-2) and E_{Corr} (corrosion potential, mV) deduced from these polarisation curves.

Figure 5b shows the polarisation curves recorded for the specimens when tested against Hank's solution. In the case of the untreated alloy, similar to the performance against 3.5% NaCl solution, a stable passive domain was observed until potentials of around +150 mV. However, the E_{Corr} value was found to be significantly lower, at around -789 mV, which suggested an inferior corrosion performance as compared to against 3.5% NaCl solution.

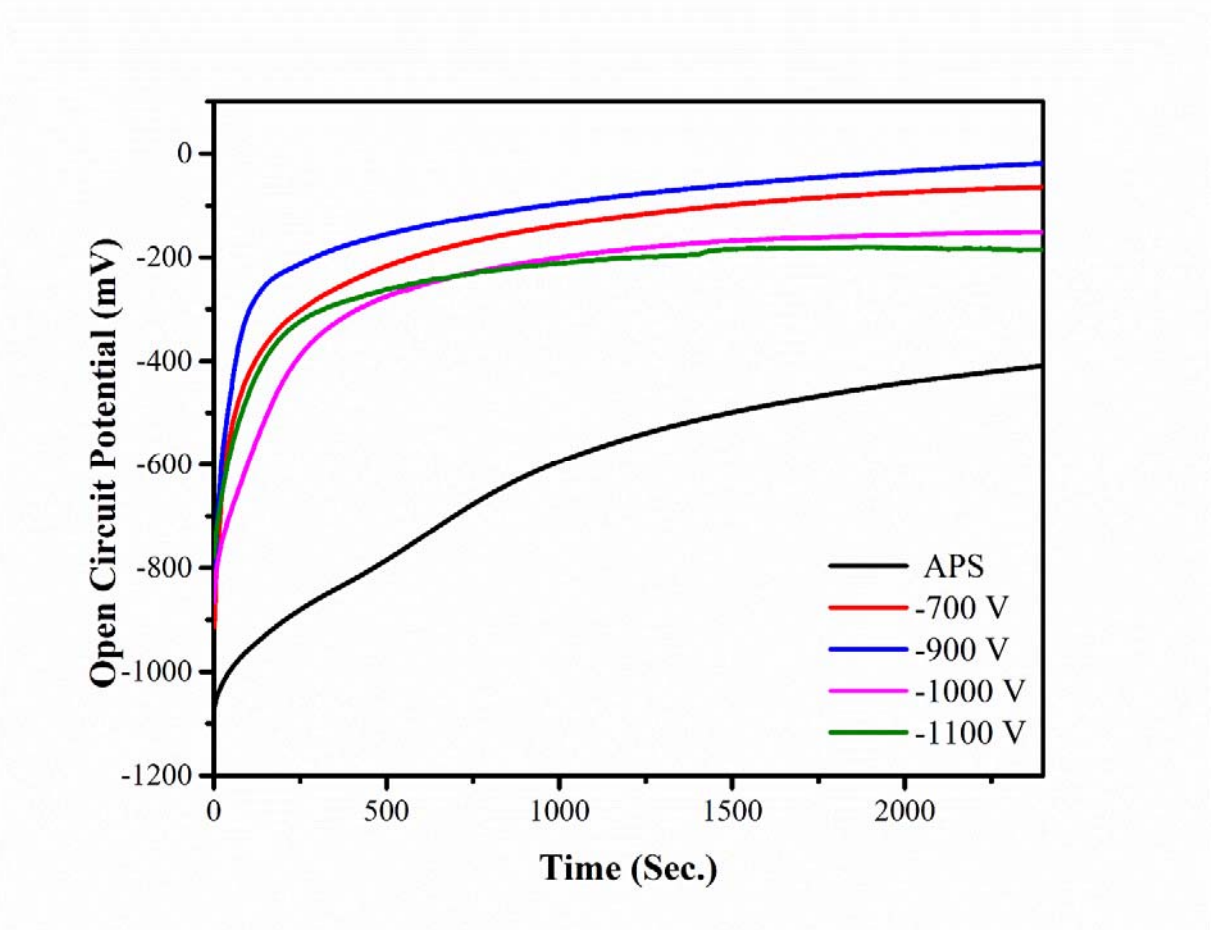
Open Circuit Potential (mV)
0
-200
-400
-600
-800
-1000
-1200
0
500
1000
1500
2000
Time (Sec.)
APS
-700 V
-900 V
-1000 V
-1100 V

(a)

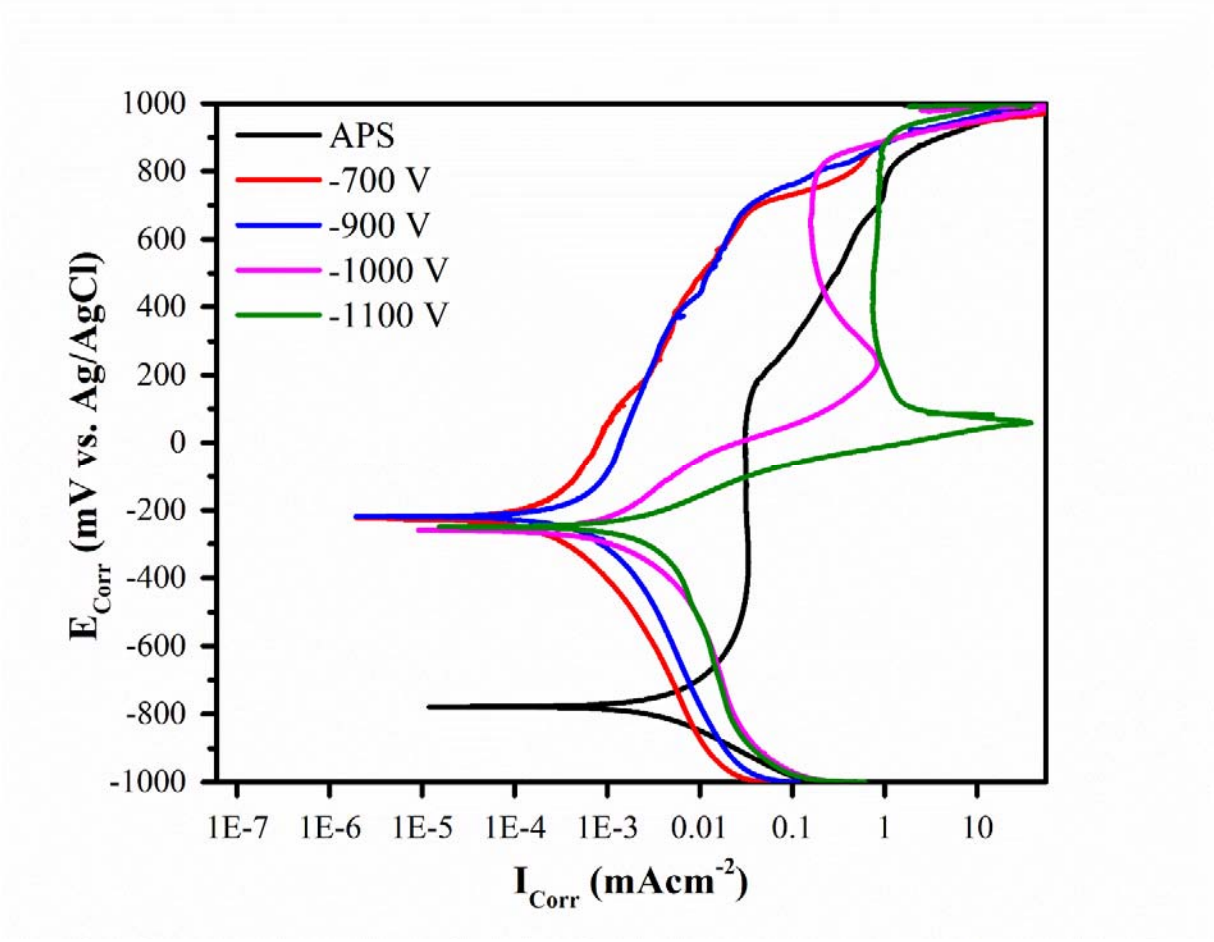

(b)

Figure 5: (a) Open circuit potential curve and (b) Potentiodynamic polarisation curves of the untreated specimen and specimens nitrided at various bias voltage (-700 V to -1100 V) in Hank's solution.

Dissolution of CoCrMo alloy has been considered sensitive to a number of factors such as the type of BSF, it's pH value, protein build-up, oxidation reactions and consequent changes in electrochemical potentials [16], [36], [37]. Literature suggests that, on immersion in Hank's solution, Co from the alloy readily undergoes dissolution by the outward migration through the passive layers [17], [52]. Number of corrosion studies on CoCrMo alloys against serum solutions

also suggest that passive layer formation based on Co does not occur and in turn retards the formation of Cr based passive layers [16], [52]. Thus, it can be inferred that Co dissolution starts as soon as specimens are immersed into the solution due to the complex organic molecular structure. There is a consensus among researchers that Cr based oxide layers (mainly Cr_2O_3 along with some Mo oxide) once formed remain stable when in contact with the serum and only dissolve gradually [56]. Thus, the observed complex behaviour of the untreated CoCrMo alloy, consisting of stable passive domain but a higher dissolution current observed in this study against Hank's solution, could be attributed to the passive layers based on Cr but along with the dissolution of Co. In the transpassive region (beyond +150 mV), the rapid rise in the corrosion current could be attributed to a number of complex phenomena consisting of formation of Cr (VI) species in the passive layers, increasing fraction of CoO and Mo (up to around 0.79 mV), dissolution of Co beyond 0.79 mV, significant increase in the passive layer thickness and water oxidation reactions [34], [37], [50].

Figure 6 shows the surface of the untreated CoCrMo alloy after the potentiodynamic polarisation tests against Hank's solution. Figure 6a shows the optical microscopic image of a partially exposed and partially unaffected (which was masked) as-polished surface. Porosity associated with the manufacturing technology of the alloy could be observed prominently in both the areas. The area exposed to the solution (figure 6a and 6b) during the test clearly showed a preferential dissolution of the ε and γ phases (as compared to the carbides) along with the eventually protruded but somewhat less corroded $M_{23}C_6$ carbide dendrites. Thus, the Cr oxide based passive layers along with the relatively inert $M_{23}C_6$ offered some protection from corrosion.

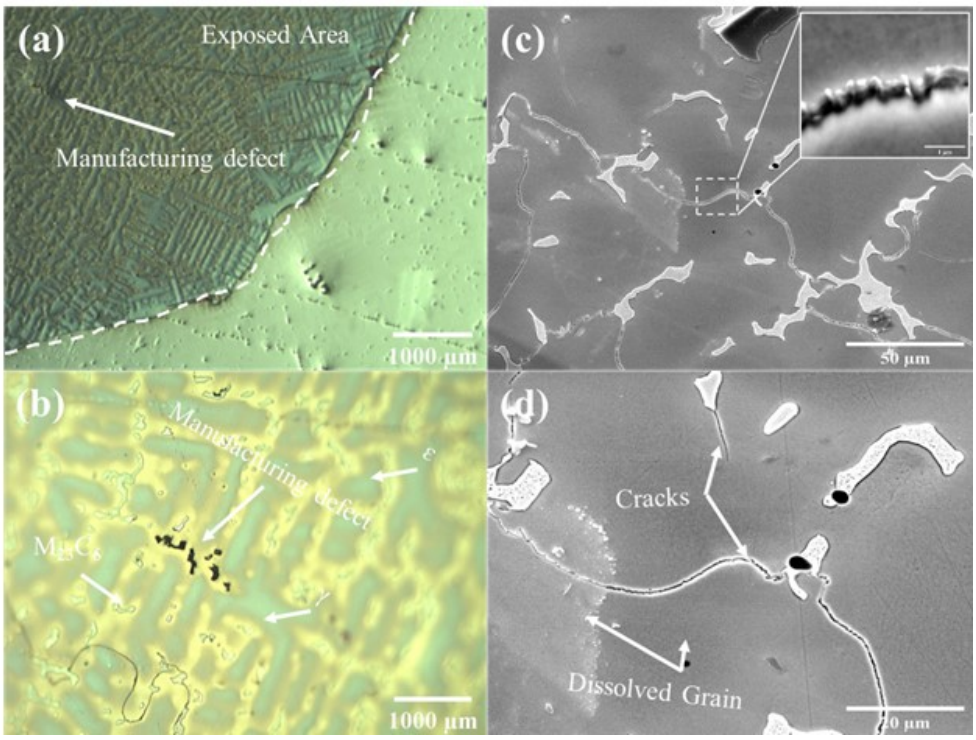

Figure 6: (a-b) Optical micrograph (c-d) SEM plan view of exposed area of the untreated alloy in Hank's solution at room temperature.

Raman analysis of this exposed area confirmed the formation of Cr and Mo based oxides (figure 10). These results were found to be consistent with the literature and with the higher anodic tranpassive dissolution currents recorded in this study. SEM images (Figure 6c and d) show this exposed area at higher magnification. No pitting was found within the exposed area. However, transgranular micro-cracks, presumably abetted by stress-corrosion (due to residual stress), linking the spaced-out metal carbides within the grains could also be observed in both these images. The presence of these cracks suggests that apart from matrix dissolution, abrupt removal of more corrosion resistant carbides due to matrix cracking could also act as an additional material removal mechanism. It is worth mentioning, that these cracks appear thicker than the

passive layers, which are estimated to be a few nanometer thick, suggesting that they ran deeper into the underneath grains.

Table 3 provides the E_{Corr} and the I_{Corr} values extracted from the polarisation curves of all the specimens when analysed against Hank's solution. A marked improvement in E_{Corr} values of the nitrided specimens (in the range of 500 mV noble compared to untreated alloy) could be observed clearly. Contrary to the results obtained against 3.5% NaCl solution, nitriding voltage did not show a clear bearing on the improvements in the E_{Corr} values. In general, the shape of the polarisation curves, especially samples nitrided at the higher voltages (-1000 V and -1100 V) mostly resembled with those obtained against the NaCl solution.

Electrolyte	**SBF (Hank's Solution)**					
Repetition	**SET-1**			**SET-2**		
Sample ID	**E_{Corr} (mV)**	**I_{Corr} ($mAcm^{-2}$)**	**OCP (mV)**	**E_{Corr} (mV)**	**I_{Corr} ($mAcm^{-2}$)**	**OCP (mV)**
Untreated	-776.37	$2.42E^{-03}$	-776.54	-762.53	$2.50E^{-03}$	-737.50
-700 V	-222.67	$1.63E^{-04}$	-61.56	-231.36	$1.52E^{-04}$	-62.25
-900 V	-218.43	$4.12E^{-04}$	-19.31	-205.19	$3.18E^{-04}$	-55.61
-1000 V	-259.51	$6.58E^{-04}$	-149.27	-243.01	$6.92E^{-04}$	-155.36
-1100 V	-249.51	$4.00E^{-03}$	-182.65	-240.02	$3.61E^{-03}$	-197.46

Table 3: OCP and polarisation data obtained from the polarisation curves of the nitrided specimens and the untreated specimen in Hank's solution (0.9 wt.% NaCl). All the electrochemical potentials reported are with respect to Ag/AgCl reference electrode.

A significant influence of the nitriding process (voltage and hence microstructure) can be observed on the corrosion currents recorded. According to the corrosion currents recorded until around +800 mV, the results could be divided into two categories. One: results which had significantly lower anodic corrosion currents; namely specimens nitrided at low voltages (-700V and -900V). And secondly: results which show higher corrosion currents amid a stable passivation domain; namely samples nitrided at higher voltages (-1000 V and -1100V).

As described in section 3.1, the microstructure of nitrided layer for -770 V and -900 V samples (figure 3) predominately consisted of a distinct, uniform S phase band at the interface of the base alloy followed by a compound layer consisting of both $M_{2\text{-}3}N$ and M_4N (where M is mostly Co dominated) amid slight differences in thickness. Despite the solution being made up of several inorganic salts and aggressive chloride and sulphate ions, the beneficial effect of the diffusion-based S phase and the $Co_{2\text{-}3}N + Co_4N$ compound layer in retarding the dissolution of the passive layers and the outward diffusion of Co was clearly evident from the polarization curves.

Figure 7 shows the SEM images of the corroded surfaces of the samples nitrided at -700 V and -900 V specimens.

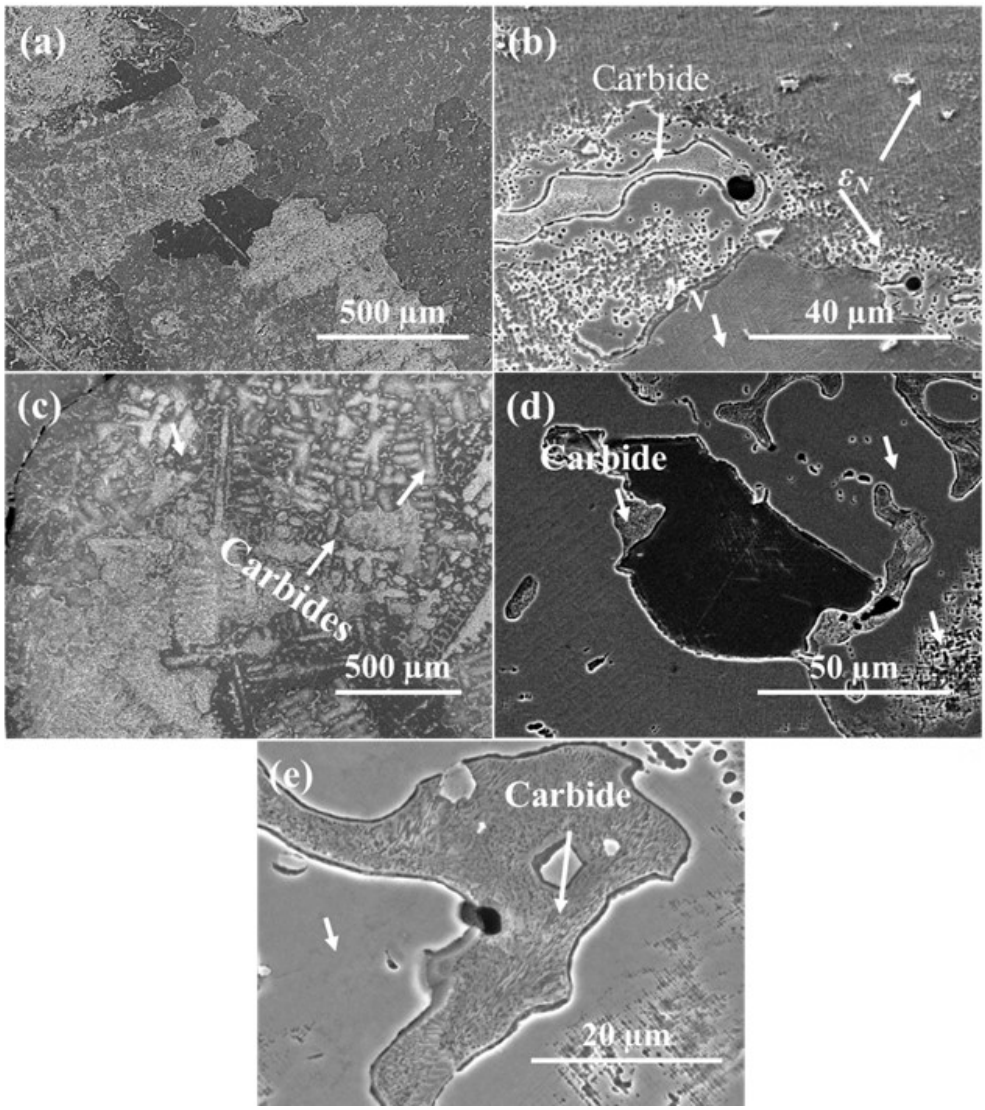

Figure 7: SEM plan view images of the corroded areas (a) -700 V sample: centre of the exposed area (b) high magnification image of corroded metal carbide (c) -900 V sample (d-e) area depicting the intersection of γ_N and metal carbide after potentiodynamic polarisation test in Hank's solution.

The low magnification SEM image of the corroded surface of the -700 V nitrided sample (figure 7a) shows different grains with a varying degree of corrosion intensity, however, exposing the partially dissolved metal carbides, most of them protruding prominently from the surrounding

matrix, irrespective of their concentration in the grains. Figure 7b shows the corroded surface at a higher magnification of the same sample. The image focuses on a metal carbide surrounded by a ϵ_N and a γ_N grain. Extensive preferential dissolution of a ϵ_N grain (grain boundary) and the metal carbide interface could be observed along with extensive micro pitting in the ϵ_N grain in the immediate vicinity of the metal carbide. Similar results of preferential dissolution of grain boundaries surrounding the metal carbides (due to Cr denudation leading to enhanced galvanic effects) have been reported before [57]. Inherent porosity arising from the manufacturing technology could also be observed. In general, the γ_N grains exhibited negligible changes in spatial features suggesting a gradual corrosion of these which was consistent with the gradual rise in the corrosion currents observed in the polarisation curve recorded for this sample. Figure 7(c-e) shows the corroded surface of the -900 V nitrided sample. In this case as well, preferential dissolution of the ϵ_N grains resulting in the carbides being exposed (figure 8c), preferential dissolution of the interface of metal carbide and ϵ_N grain (figure 7(d-e)) could be observed prominently. Table 4 gives the atomic percentage (at%) of Cr and N measured in the γ_N and the ϵ_N grains of the uncorroded nitrided specimens in this study with the help of the EDS technique. The results suggest that the ϵ_N grains are depleted of Cr as compared to the γ_N grains. This could explain the preferential dissolution of the ϵ_N since they lose out on the protective Cr oxide based passive layer formation [58]. The lower corrosion rate of the -700V and -900 V nitrided samples as compared to the untreated could be thus attributed to corrosion resistant γ_N grains and to some extent to the thicker 'S' phase diffusion layer (around 123-283nm).

Sample ID		Phases (at. %)	
		γ_N	ε_N
-700 V	Cr	24.9 ± 0.34	23.6 ± 0.32
	N	26.9 ± 0.26	29.1 ± 0.03
-900 V	Cr	25.5 ± 0.15	24.4 ± 0.21
	N	26.5 ± 0.08	23.2 ± 0.17
-1000 V	Cr	24.3 ± 0.14	23.9 ± 0.16
	N	24.7 ± 0.28	25.6 ± 0.50
-1100 V	Cr	26.16 ± 0.14	24.2 ± 0.19
	N	20.56 ± 0.21	25.23 ± 0.19

Table 4: Elemental composition in terms of Cr and N content measured in the γ_N and the ε_N grains with the help of EDX technique.

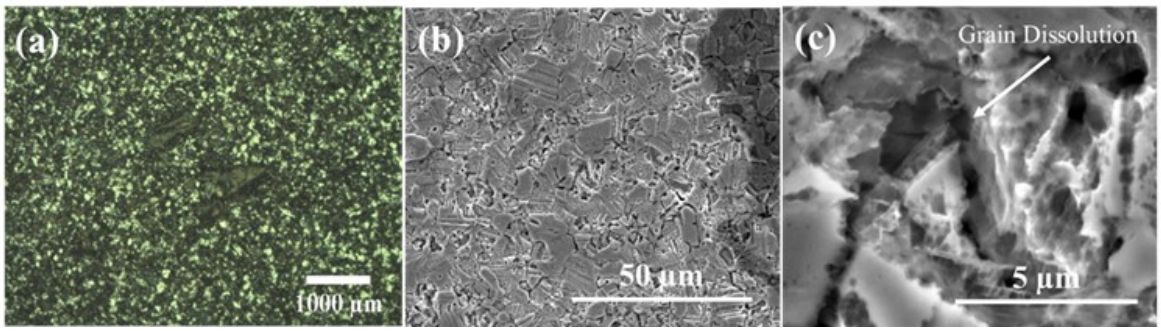

Figure 8: (a) Bright field optical micrograph of the -1000 V sample (b) SEM plan view of centre of exposed area of sample and (c) SEM plan view of dissolved grain boundary area along the ϵ_N grains at higher magnification.

Figure 8 shows the exposed surface area of sample nitrided at -1000 V after potentiodynamic polarisation test in Hank's solution. At low magnification, the microstructure of the sample showed random distribution of fine grains of ϵ_N (dark constrast) γ_N (bright contrast) phases (figure 8a). The dark contrast in the bright field optical image was due to the scattering of light associated with roughness due to corrosion. Figure 8 (b) shows the SEM image of this corroded area at higher magnification. On a closer look, significant dissolution of the grain boundaries, preferably along the ϵ_N grains could be prominently observed. Literature suggests that any precipitation of CrN/Cr_2N will happen along the grain boundaries [59], [60]. Figure 8c shows such a dissolved area near the grain boundaries at a higher magnification. It revealed that these terminate into pits which run deeper into the specimen, presumably breach the diffusion-based S phase layer and reach untreated alloy with the passage of time. It could also be speculated that, the application of higher nitriding voltages, results in S phase diffusion layer with higher defect densities due to the more intensive ion bombardment. XRD results also suggested that higher nitriding voltages (>1000 V and -1100 V in this case) promoted the formation of ϵ_N phase. Thus, the poor corrosion resistance of the ϵ_N grains along with the amplified galvanic effects due to compositional changes associated with nitride precipitation along the grain boundaries could be attributed to the enhanced corrosion of these areas. This is consistent with the steep rise of corrosion currents recorded for this sample from the E_{Corr} to almost +200 mV (figure 5b). The sharp passivation domain seen from around +200 mV to around +800 mV could be thus attributed to the response from the corrosion resistant S phase [53] (albeit thinner than the previous two samples) and the freshly exposed base alloy.

Figure 9 shows the corroded areas of the sample nitrided at -1100 V. As evident from the bright and dark contrast areas in the optical image 9 (a), the corrosion performance and mechanism of

this sample resembled to that of the -1000 V. Figure 9 (b), shows a pit formed at the junction of three different grains due to preferential dissolution. Apart from the grain boundary dissolution mechanism, intergranular cracks were also found for this sample. XRD results showed that this sample had the maximum lattice expansion due to higher nitrogen incorporation along with the preferred formation of ϵ_N phase [1]. Thus, the cracking could be attributed to higher intrinsic stress of the nitrided layer facilitated by corrosion (stress-corrosion), which in turn contributed to the higher corrosion currents by providing the solution a direct path to the areas below.

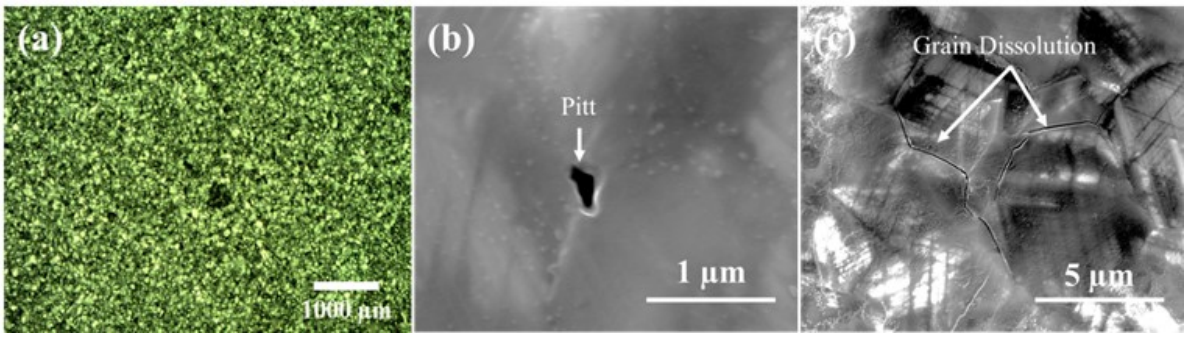

Figure 9: Corroded area of the sample nitrided at -1100 V; (a) Optical micrograph of the corroded area (b) SEM image of pit formed near the grain boundaries (c) Intergranular cracking.

Figure 10 exhibits the Raman spectra of the nitrided, and untreated specimens obtained from different sections of the corroded area (which were peculiar and anticipated to be associated with the formation of corrosion products). It was clear from the Raman spectra, that all the specimens indicated the formation of metal oxides (MOs) mainly based on Cr and Mo. No evidence of Co based oxides was found throughout the exposed area, which reiterated that Co did not form oxides which reaffirms results available through the literature.

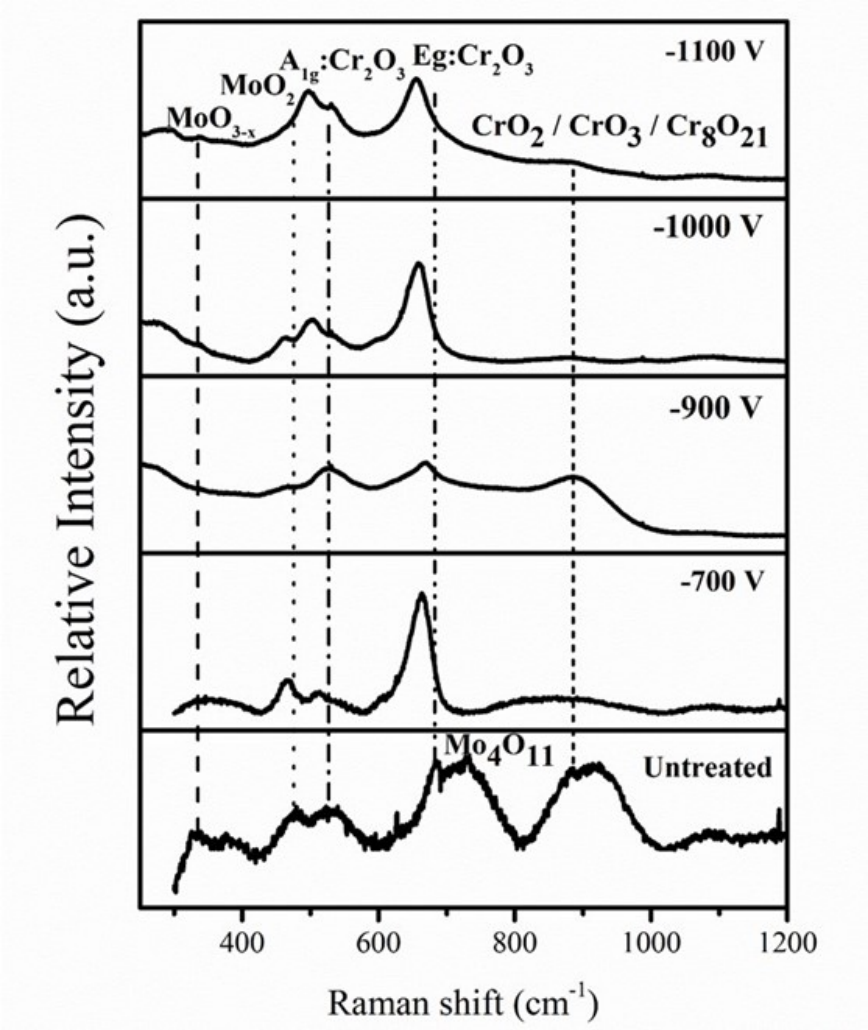

Figure 10: Raman spectra obtained from the corroded areas of the untreated and the nitrided alloys.

From the figure 10, it could be seen that no phases of any MOs were observed in the frequency range of 200-400 cm^{-1} for untreated alloy. After 400 cm^{-1} frequency, peaks related to CrO_2, MoO_2 (Eg band), Cr_2O_3 (both A_{1g} and E_g band), CrO_2 (B_{2g} band), CrO_3, Cr_8O_{21} and Mo_4O_{11} could be observed [61], [62], [63], [64], [65], [66], [67], [68], [69], [70], [71], [72]. Most of these peaks originated from the areas near the γ_N and carbides. However, no clear peaks on ϵ_N phases were found. Even though the intensity of the Cr_2O_3 and CrO_2/MoO_2 peaks changed as the sample

was scanned from different areas within the corroded portions, the nature and the combination of the phase remained the same.

Raman spectra obtained for nitrided specimen hinted the formation of different Cr and Mo oxides. As it could be seen form the figure 10, Cr_2O_3 phase dominated in all nitrided specimens. The highest intensity of Cr_2O_3 was observed in the case of -700 V which corresponded to Eg bending. Whereas, for -900 V sample, both A_{1g} and E_g bending of Cr_2O_3 contributed the most compared to other Cr and Mo oxide phases. Apart from these phases, spectra of nitrided specimens were also found to have three extra MO peaks which were observed at the start of the scan (200-400 cm^{-1}). As presented in table 5, these peaks corresponded to the formation of MoO_3, CrO_4 and CrO_6 and correlates to the v_4 bending mode [70], [71]. However, peak position of these phases were slightly shifted from original position (285 cm^{-1} B_{2g}: δ O=M=O, wagging) [70]. Peak shifting is often associated with the roughness of the exposed area due to the multiple scattering of phonons. Surprisingly, both CrO_4 and CrO_6 phases were not observed for the -700 V and -1000 V samples. On the other hand, MoO_3 was observed for all sample nitrided at higher voltage (≥ -900 V). At the same time, no evidence of CrO_2 (B_{2g}) and Mo_4O_{11} was found in any of nitrided specimens. At the end of the spectra, a board peak (frequency range between 800 to 900 cm^{-1}) was observed which corresponded to amorphous Cr oxides.

Some of the peaks were found to have similar frequency as other phases such as CrO_3 or $Cr_8O_{21}$and Mo_4O_{11} which have orthorhombic crystal structure. The peak at 907 cm^{-1} corresponded to both CrO_3 and Mo_4O_{11}, whereas this peak (Mo_4O_{11}) attributed to terminal Mo-O vibration. Interestingly, Raman peaks related to Co oxides (balanced element) were not found which indicated that Co mainly dissolves during the tests into electrolyte (Hank's solution). Likewise, CrO and MoO phases were absent and could not be indexed.

Type of Metal Oxide	APS	Sample A	Sample B	Sample C	Sample D
MoO_{3-x}			274.6	280.19	287.41
CrO_4 (v_4 bending)			335.53		337.93
CrO6 (v_4 bending)			391.66		387.83
CrO_2 (E_g)	479.92	464.3	465.44	472.65	497.51
MoO_2 (E_g)	508.08	514.3		516.76	
Cr_2O_3 (A_{1g})	522.94		526.38		531.19
	540.15	540.9			
Cr_2O_3 (E_g)	626.98	627		609.78	
	634.81	663.8	668.32		654.59
	683.31	665.3		675.54	
CrO_2 (B_{2g})	702.86				
	709.09				
Mo_4O_{11}	733.37				
	746.68				
CrO_3 or Cr_8O_{21}	829.59	857			
	885.92	862.5	886.45	878.43	870.41
Mo_4O_{11}	907.82				
	923.47				

Table 5: Raman spectra obtained from the corroded area of the untreated and the nitrided alloys.

4 Conclusions

The current work demonstrated that the HIPIMS technique could be effectively used for nitriding CoCrMo alloys in order to improve its corrosion resistance. The corrosion performance, in both cases of 3.5% wt NaCl and Hank's solution, was sensitive to the microstructure of the untreated and the nitrided alloys, which in turn could be controlled by varying the nitriding voltage. From this study the following important inferences could be drawn:

1. The thickness and the composition of the nitrided layer changed with an increase in bias voltage (Ub= -700 V to -1100 V) and reached around 5 microns for samples nitrided at -1100 V.
2. A significant improvement in the E_{Corr} values was observed irrespective of the nitriding voltage as compared to the untreated alloys.
3. Microstructure played a significant role in determining the corrosion resistance, wherein the ϵ_N grains and the grain boundaries seemed to preferentially corrode as compared to the γ_N grains. Also, precipitation of Cr based nitrides (CrN and Cr_2N) observed for higher nitriding voltages of -1000 V and -1100 V deteriorated the corrosion resistance of the nitrided alloy.
4. The nitrided alloy appeared to draw its corrosion resistance from the corrosion resistant γ_N grains and the diffusion-based S phase layers. CS-SEM studies revealed that this layer was thickest in the case of -900 V.
5. The specimens nitrided at -900 V exhibited the best corrosion resistance followed by the those nitrided at -700 V in both test environments. This could be attributed due to right combination of a thicker S phase diffusion-based layer at the substrate interface and a

compound layer ($M_{2-3}N$ and M_4N, where M= is mainly Co dominated) which produced Cr + Mo based passive layers when subjected to corrosive conditions.

5 Acknowledgement:

Authors would like to acknowledge Zimmer-Biomet, UK for providing financial support to carryout doctoral research of one of the authors, Krishnanand Shukla.

6 Authors Contribution:

Krishnanand S. P. Shukla: Experimental work, data collection, processing and analyses, draft preparation. **Yashodhan P. Purandare:** Experimental work, processing and analyses, draft preparation. **Arunprabhu A. Sugumaran:** Nitriding experimental work **A. P. Ehiasarian:** Leading the HIPIMS research, results interpretation, and draft verification. **Imran Khan:** Defining the research idea, **P. Eh Hovsepian:** Defining the research idea, Technology and material development, Supervision, and scientific interpretation of the experimental results.

7 References

[1] K. Shukla, A. A. Sugumaran, I. Khan, A. P. Ehiasarian, and P. E. Hovsepian, "Low pressure plasma nitrided CoCrMo alloy utilising HIPIMS discharge for biomedical applications," *J. Mech. Behav. Biomed. Mater.*, vol. 111, no. August, p. 104004, 2020, doi: 10.1016/j.jmbbm.2020.104004.

[2] N. Palaniappan, G. K. Inwati, and M. Singh, "Biomaterial Co-Cr-Mo alloys nano coating calcium phosphate orthopedic treatment," in *IOP Conference Series: Materials Science*

and Engineering, Aug. 2014, vol. 64, no. 1, p. 012026, doi: 10.1088/1757-899X/64/1/012026.

[3] H. D. Ran Liu, Xiaoying Li □, Xiao Hu, "Surface modification of a medical grade Co□Cr□Mo alloy by low-temperature plasma surface alloying with nitrogen and carbon," *Surf. Coatings Technol. J.*, vol. 232, pp. 906–911, 2013, [Online]. Available: https://pdf.sciencedirectassets.com/271621/1-s2.0-S0257897213X00209/1-s2.0-

[4] N. Tang, Y. Li, Y. Koizumi, and A. Chiba, "Nitriding of Co-Cr-Mo alloy in nitrogen," *Mater. Chem. Phys.*, vol. 145, no. 3, pp. 350–356, 2014, doi: 10.1016/j.matchemphys.2014.02.023.

[5] S. M. T. Chan, C. P. Neu, K. Komvopoulos, A. H. Reddi, and P. E. Di Cesare, "Friction and wear of hemiarthroplasty biomaterials in reciprocating sliding contact with articular cartilage," *J. Tribol.*, vol. 133, no. 4, pp. 1–7, 2011, doi: 10.1115/1.4004760.

[6] C. Stotter *et al.*, "Effects of Loading Conditions on Articular Cartilage in a Metal□on□Cartilage Pairing," *J. Orthop. Res.*, vol. 37, no. 12, pp. 2531–2539, Dec. 2019, doi: 10.1002/jor.24426.

[7] M. J. Nine, D. Choudhury, A. C. Hee, R. Mootanah, and N. A. A. Osman, "Wear debris characterization and corresponding biological response: Artificial hip and knee joints," *Materials (Basel).*, vol. 7, no. 2, pp. 980–1016, 2014, doi: 10.3390/ma7020980.

[8] D. De Pasquale *et al.*, "Metal-on-metal hip prostheses: Correlation between debris in the synovial fluid and levels of cobalt and chromium ions in the bloodstream," *Int. Orthop.*, vol. 38, no. 3, pp. 469–475, 2014, doi: 10.1007/s00264-013-2137-5.

[9] D. Ebreo, A. Khan, M. El-Meligy, C. Armstrong, and V. Peter, “METAL ION LEVELS AFTER REVISION SURGERY FOR METALLOSIS ARISING FROM LARGE DIAMETER METAL-ON-METAL TOTAL HIP ARTHROPLASTY OR RESURFACING ARTHROPLASTY,” *Orthop. Proc.*, vol. 94-B, no. SUPP_XXXVII, p. 224, Sep. 2012, doi: 10.1302/1358-992X.94BSUPP_XXXVII.EFORT2011-224.

[10] V. Sansone, D. Pagani, and M. Melato, “The effects on bone cells of metal ions released from orthopaedic implants. A review,” *Clin. Cases Miner. Bone Metab.*, vol. 10, no. 1, pp. 34–40, 2013, doi: 10.11138/ccmbm/2013.10.1.034.

[11] F. Noli, L. Pichon, and O. Öztürk, “The Influence of Plasma-Based Nitriding and Oxidizing Treatments on the Mechanical and Corrosion Properties of CoCrMo Biomedical Alloy,” *Metall. Mater. Trans. A Phys. Metall. Mater. Sci.*, vol. 49, no. 4, pp. 1383–1396, 2018, doi: 10.1007/s11661-018-4487-5.

[12] M. D. Dianyi Yu, “Chromium (Cr) Toxicity,” *U.S. Dep. Heal. Hum. Serv. Agency Toxic Subst. Dis. Regist. Div. Toxicol. Environ. Med. Environ. Med. Educ. Serv. Branch*, pp. 1–67, 2008, [Online]. Available: https://www.atsdr.cdc.gov/csem/chromium/docs/chromium.pdf.

[13] K. Czarnek, S. Terpilowska, and A. K. Siwicki, “Selected aspects of the action of cobalt ions in the human body,” *Cent. Eur. J. Immunol.*, vol. 40, no. 2, pp. 236–242, 2015, doi: 10.5114/ceji.2015.52837.

[14] N. Lombaert, D. Lison, P. Van Hummelen, and M. Kirsch-Volders, “In vitro expression of hard metal dust (WC-Co) - responsive genes in human peripheral blood mononucleated cells,” *Toxicol. Appl. Pharmacol.*, vol. 227, no. 2, pp. 299–312, 2008, doi:

10.1016/j.taap.2007.11.002.

[15] I. Campos-Silva, D. Bravo-Bárcenas, H. Cimenoglu, U. Figueroa-López, M. Flores-Jiménez, and O. Meydanoglu, "The boriding process in CoCrMo alloy: Fracture toughness in cobalt boride coatings," *Surf. Coatings Technol.*, vol. 260, pp. 362–368, 2014, doi: 10.1016/j.surfcoat.2014.07.092.

[16] F. Contu, B. Elsener, and H. Böhni, "Corrosion behaviour of CoCrMo implant alloy during fretting in bovine serum," *Corros. Sci.*, vol. 47, no. 8, pp. 1863–1875, 2005, doi: 10.1016/j.corsci.2004.09.003.

[17] T. Hanawa, S. Hiromoto, and K. Asami, "Characterization of the surface oxide film of a Co-Cr-Mo alloy after being located in quasi-biological environments using XPS," *Appl. Surf. Sci.*, vol. 183, no. 1–2, pp. 68–75, 2001, doi: 10.1016/S0169-4332(01)00551-7.

[18] J. A. Ortega-Saenz, M. A. L. Hernandez-Rodriguez, V. Ventura-Sobrevilla, R. Michalczewski, J. Smolik, and M. Szczerek, "Tribological and corrosion testing of surface engineered surgical grade CoCrMo alloy," *Wear*, 2011, doi: 10.1016/j.wear.2010.12.062.

[19] Y. N. Petrov *et al.*, "Influence of microstructural modifications induced by ultrasonic impact treatment on hardening and corrosion behavior of wrought Co-Cr-Mo biomedical alloy," *Mater. Sci. Eng. C*, vol. 58, pp. 1024–1035, 2016, doi: 10.1016/j.msec.2015.09.004.

[20] X. Z. Xin, N. Xiang, J. Chen, and B. Wei, "In vitro biocompatibility of Co-Cr alloy fabricated by selective laser melting or traditional casting techniques," *Mater. Lett.*, vol. 88, pp. 101–103, 2012, doi: 10.1016/j.matlet.2012.08.032.

[21] M. ASLAN, O. ÇOMAKLI, M. YAZICI, A. F. YETIM, Ö. BAYRAK, and A. ÇELIK, "THE EFFECT OF PLASMA OXIDATION AND NITRIDATION ON CORROSION BEHAVIOR OF CoCrMo ALLOY IN SBF SOLUTION," *Surf. Rev. Lett.*, vol. 25, no. 08, p. 1950024, Dec. 2018, doi: 10.1142/S0218625X19500240.

[22] D. C. Ba, L. Xu, and Q. Wang, "Effects of plasma nitriding ion beam flux density and time on the properties of CoCrMo alloy," *Vacuum*, vol. 119, pp. 214–222, 2015, doi: 10.1016/j.vacuum.2015.05.032.

[23] O.ÖztürkaS.OkuraL.PichonbM.O.LiedkecJ.P.Riviereb, "Magnetic layer formation on plasma nitrided CoCrMo alloy," *Surf. Coatings Technol.*, vol. 205, Suppl, pp. S280–S285, 2011, doi: doi:10.1016/j.surfcoat.2011.01.047.

[24] P. E. Hovsepian, A. A. Sugumaran, Y. Purandare, D. A. L. Loch, and A. P. Ehiasarian, "Effect of the degree of high power impulse magnetron sputtering utilisation on the structure and properties of TiN films," *Thin Solid Films*, vol. 562, pp. 132–139, 2014, doi: 10.1016/j.tsf.2014.04.002.

[25] V. Ragone *et al.*, "CoCrMo alloys ions release behavior by TiNbN coating: an in vitro study," *Biomed. Microdevices*, vol. 21, no. 3, p. 61, 2019, doi: 10.1007/s10544-019-0417-6.

[26] P. E. Hovsepian and A. P. Ehiasarian, "Six strategies to produce application tailored nanoscale multilayer structured PVD coatings by conventional and High Power Impulse Magnetron Sputtering (HIPIMS)," *Thin Solid Films*, vol. 688, no. July, p. 137409, 2019, doi: 10.1016/j.tsf.2019.137409.

[27] P. E. Hovsepian, A. P. Ehiasarian, Y. Purandare, A. A. Sugumaran, T. Marriott, and I. Khan, “Development of superlattice CrN/NbN coatings for joint replacements deposited by high power impulse magnetron sputtering,” *J. Mater. Sci. Mater. Med.*, 2016, doi: 10.1007/s10856-016-5751-0.

[28] X. Luo and X. Li, “Design and characterisation of a new duplex surface system based on S-phase hardening and carbon-based coating for ASTM F1537 Co-Cr-Mo alloy,” *Appl. Surf. Sci.*, 2014, doi: 10.1016/j.apsusc.2013.11.141.

[29] A. Samanta *et al.*, “Nano- and micro-tribological behaviours of plasma nitrided Ti6Al4V alloys,” *J. Mech. Behav. Biomed. Mater.*, vol. 77, pp. 267–294, 2018, doi: 10.1016/j.jmbbm.2017.09.013.

[30] N. Mingolo, A. P. Tschiptschin, and C. E. Pinedo, “On the formation of expanded austenite during plasma nitriding of an AISI 316L austenitic stainless steel,” *Surf. Coatings Technol.*, vol. 201, no. 7 SPEC. ISS., pp. 4215–4218, 2006, doi: 10.1016/j.surfcoat.2006.08.060.

[31] A. Samanta *et al.*, “Nanotribological response of a plasma nitrided bio-steel,” *J. Mech. Behav. Biomed. Mater.*, vol. 65, pp. 584–599, Jan. 2017, doi: 10.1016/j.jmbbm.2016.09.017.

[32] K. Shukla, Y. P. Purandare, I. Khan, A. P. Ehiasarian, and P. E. H. Hovsepian, “Effect of nitriding voltage on the impact load fatigue and fracture toughness behaviour of CoCrMo alloy nitrided utilising a HIPIMS discharge,” *Surf. Coatings Technol.*, vol. 400, p. 126227, Oct. 2020, doi: 10.1016/j.surfcoat.2020.126227.

[33] H. Dong, "S-phase surface engineering of Fe-Cr, Co-Cr and Ni-Cr alloys," *Int. Mater. Rev.*, vol. 55, no. 2, pp. 65–98, Mar. 2010, doi: 10.1179/095066009X12572530170589.

[34] A. Bazzoni, S. Mischler, and N. Espallargas, "Tribocorrosion of Pulsed Plasma-Nitrided CoCrMo Implant Alloy," *Tribol. Lett.*, vol. 49, no. 1, pp. 157–167, Jan. 2013, doi: 10.1007/s11249-012-0047-0.

[35] J. Lutz, C. Díaz, J. A. García, C. Blawert, and S. Mändl, "Corrosion behaviour of medical CoCr alloy after nitrogen plasma immersion ion implantation," *Surf. Coatings Technol.*, vol. 205, no. 8–9, pp. 3043–3049, Jan. 2011, doi: 10.1016/j.surfcoat.2010.11.017.

[36] Y. Liu and B. Chen, "In vivo corrosion of CoCrMo alloy and biological responses: a review," *Mater. Technol.*, vol. 33, no. 2, pp. 127–134, 2018, doi: 10.1080/10667857.2017.1408929.

[37] N. Espallargas, C. Torres, and A. I. Muñoz, "A metal ion release study of CoCrMo exposed to corrosion and tribocorrosion conditions in simulated body fluids," *Wear*, vol. 332–333, pp. 669–678, 2015, doi: 10.1016/j.wear.2014.12.030.

[38] A. A. Sugumaran, K. Shukla, I. Khan, A. P. Ehiasarian, and P. E. Hovsepian, "Dry sliding wear mechanisms of HIPIMS plasma nitrided CoCrMo alloy for medical implant applications," *Vacuum*, vol. 185, no. December 2020, p. 109994, Mar. 2021, doi: 10.1016/j.vacuum.2020.109994.

[39] A. P. Ehiasarian, J. G. Wen, and I. Petrov, "Interface microstructure engineering by high power impulse magnetron sputtering for the enhancement of adhesion," *J. Appl. Phys.*, vol. 101, no. 5, p. 054301, Mar. 2007, doi: 10.1063/1.2697052.

[40] W.-D. M. A. P. Ehiasarian, P. Eh. Hovsepian, “A Combined Process Comprising Magnetic Field-Assisted, High-Power, Pulsed Cathode Sputtering and an Unbalanced Magnetron,” US 10718435, 2005, EP 1 260 603 A2, DE 10124749, 21.05. 2001, 2005.

[41] P. Ehiasarian Hovsepian, A. Papken Ehiasarian, Y. Purandare, A. Arunachalam Sugumaran, T. Marriott Zimmer Biomet, and I. Khan Zimmer Biomet, “Development of superlattice CrN/NbN coatings for joint replacements deposited by High Power Impulse Magnetron Sputtering.”

[42] D. D. A.P. Ehiasarian, R.Tietema, R. Bugyi, A. Klimczak, P. Eh. Hovsepian, “A vacuum treatment apparatus, a bias power supply and a method of operating a vacuum treatment apparatus,” 2011.

[43] J. V. Giacchi, C. N. Morando, O. Fornaro, and H. A. Palacio, “Microstructural characterization of as-cast biocompatible Co-Cr-Mo alloys,” *Mater. Charact.*, vol. 62, no. 1, pp. 53–61, 2011, doi: 10.1016/j.matchar.2010.10.011.

[44] J. B. Park, K.-H. Jung, K. M. Kim, Y. Son, J.-I. Lee, and J. H. Ryu, “Microstructure of As-cast Co-Cr-Mo Alloy Prepared by Investment Casting,” *J. Korean Phys. Soc.*, vol. 72, no. 8, pp. 947–951, 2018, doi: 10.3938/jkps.72.947.

[45] S. Mineta, Alfirano, S. Namba, T. Yoneda, K. Ueda, and T. Narushima, “Phase and morphology of carbides in ASTM F75 Co-Cr-Mo-C alloys formed at 1473 to 1623 K,” *Mater. Sci. Forum*, vol. 654–656, pp. 2176–2179, 2010, doi: 10.4028/www.scientific.net/MSF.654-656.2176.

[46] A. Çelik, Ö. Bayrak, A. Alsaran, I. Kaymaz, and A. F. Yetim, “Effects of plasma nitriding

on mechanical and tribological properties of CoCrMo alloy," *Surf. Coatings Technol.*, vol. 202, no. 11, pp. 2433–2438, 2008, doi: 10.1016/j.surfcoat.2007.08.030.

[47] R. Liu, "Surface Modification of ASTM F-1537 Co-Cr Alloy by Low Temperature Plasma Surface Alloying," The University of Birmingham, 2013.

[48] K. Shukla, A. A. Sugumaran, I. Khan, A. P. Ehiasarian, and P. E. Hovsepian, "Low pressure plasma nitrided CoCrMo alloy utilising HIPIMS discharge for biomedical applications," *J. Mech. Behav. Biomed. Mater.*, vol. 111, p. 104004, Nov. 2020, doi: 10.1016/j.jmbbm.2020.104004.

[49] T. Bell, "Surface engineering of austenitic stainless steel," *Surf. Eng.*, vol. 18, no. 6, pp. 415–422, Dec. 2002, doi: 10.1179/026708402225006268.

[50] I. Milošev and H. H. Strehblow, "The composition of the surface passive film formed on CoCrMo alloy in simulated physiological solution," *Electrochim. Acta*, vol. 48, no. 19, pp. 2767–2774, 2003, doi: 10.1016/S0013-4686(03)00396-7.

[51] Y. S. Li, R. Wang, P. He, B. X. Huang, and P. Kovacs, "Surface-enhanced Raman spectroelectrochemical studies of corrosion films on implant Co-Cr-Mo alloy in biosimulating solutions," *J. Raman Spectrosc.*, vol. 30, no. 2, pp. 97–103, 1999, doi: 10.1002/(SICI)1097-4555(199902)30:2<97::AID-JRS352>3.0.CO;2-X.

[52] M. Pourbaix, *Atlas of electrochemical equilibria in aqueous solutions. Houston:NACE International*. 1974.

[53] G. Aldrich-Smith, D. G. Teer, and P. A. Dearnley, "Corrosion-wear response of sputtered CrN and S-phase coated austenitic stainless steel," *Surf. Coatings Technol.*, vol. 116–119,

pp. 1161–1165, 1999, doi: 10.1016/S0257-8972(99)00222-4.

[54] A. Jain, “Body fluid composition,” *Pediatr. Rev.*, vol. 36, no. 4, pp. 141–152, Apr. 2015, doi: 10.1542/pir.36-4-141.

[55] K. Shukla, R. Rane, J. Alphonsa, P. Maity, and S. Mukherjee, “Structural, mechanical and corrosion resistance properties of Ti/TiN bilayers deposited by magnetron sputtering on AISI 316L,” *Surf. Coatings Technol.*, vol. 324, pp. 167–174, Sep. 2017, doi: 10.1016/j.surfcoat.2017.05.075.

[56] F. Contu and B. Elsener H Bhni, “Characterization of implant materials in fetal bovine serum and sodium sulfate by electrochemical impedance spectroscopy. I. Mechanically polished samples,” *J. Biomed. Mater. Res.*, vol. 62, no. 3, pp. 412–421, Dec. 2002, doi: 10.1002/jbm.10329.

[57] Y. Liu and J. L. Gilbert, “Effect of simulated inflammatory conditions and potential on dissolution and surface oxide of CoCrMo alloy: In situ electrochemical atomic force microscopy study,” *Electrochim. Acta*, vol. 262, pp. 252–263, 2018, doi: 10.1016/j.electacta.2017.12.151.

[58] A. Martinavičius *et al.*, “Nitrogen interstitial diffusion induced decomposition in AISI 304L austenitic stainless steel,” *Acta Mater.*, vol. 60, no. 10, pp. 4065–4076, 2012, doi: 10.1016/j.actamat.2012.04.014.

[59] S. Mändl, R. Dunkel, D. Hirsch, and D. Manova, “Intermediate stages of CrN precipitation during PIII nitriding of austenitic stainless steel,” *Surf. Coatings Technol.*, vol. 258, pp. 722–726, 2014, doi: 10.1016/j.surfcoat.2014.08.007.

[60] D. Manova, D. Hirsch, J. W. Gerlach, T. Höche, S. Mändl, and H. Neumann, “Nitriding of Fe-Cr-Ni films by low energy ion implantation,” *Surf. Coatings Technol.*, vol. 202, no. 11, pp. 2443–2447, 2008, doi: 10.1016/j.surfcoat.2007.09.021.

[61] J. Singh, V. Verma, and R. Kumar, “Preparation and structural, optical studies of Al substituted chromium oxide (Cr2O3) nanoparticles,” *Vacuum*, vol. 159, no. July 2018, pp. 282–286, 2019, doi: 10.1016/j.vacuum.2018.09.033.

[62] M. Mohammadtaheri, Q. Yang, Y. Li, and J. Corona-Gomez, “The effect of deposition parameters on the structure and mechanical properties of chromium oxide coatings deposited by reactive magnetron sputtering,” *Coatings*, vol. 8, no. 3, pp. 1–14, 2018, doi: 10.3390/coatings8030111.

[63] L. Xin, Y. Lu, and T. Shoji, “The comparative study on nanostructured tribolayers of Alloy 690TT subjected to fretting wear under different oxygen contents,” *Mater. Charact.*, vol. 131, no. March, pp. 157–167, 2017, doi: 10.1016/j.matchar.2017.04.034.

[64] M. Roy, S. Ghosh, and M. K. Naskar, “Solvothermal synthesis of Cr2O3 nanocubes via template-free route,” *Mater. Chem. Phys.*, vol. 159, pp. 101–106, 2015, doi: 10.1016/j.matchemphys.2015.03.058.

[65] S. Kikuchi, K. Kawauchi, M. Kurosawa, H. Honjho, and T. Yagishita, “Non-destructive rapid analysis discriminating between chromium(VI) and chromium(III) oxides in electrical and electronic equipment using Raman spectroscopy,” *Anal. Sci.*, vol. 21, no. 3, pp. 197–198, 2005, doi: 10.2116/analsci.21.197.

[66] O. Monnereau *et al.*, “Chromium oxides mixtures in PLD films investigated by Raman

spectroscopy," *J. Optoelectron. Adv. Mater.*, vol. 12, no. 8, pp. 1752–1757, 2010.

[67] M. N. Iliev, A. P. Litvinchuk, H. G. Lee, C. W. Chu, A. Barry, and J. M. D. Coey, "Raman spectroscopy of ferromagnetic CrO2," *Phys. Rev. B - Condens. Matter Mater. Phys.*, vol. 60, no. 1, pp. 33–36, 1999, doi: 10.1103/PhysRevB.60.33.

[68] D. Stanoi *et al.*, "Chromium oxides thin films prepared and coated in situ with gold by pulsed laser deposition," *Mater. Sci. Eng. B Solid-State Mater. Adv. Technol.*, vol. 118, no. 1–3, pp. 74–78, 2005, doi: 10.1016/j.mseb.2004.12.016.

[69] D. A. Brown, D. Cunningham, and W. K. Glass, "The infrared and Raman spectra of chromium (III) oxide," *Spectrochim. Acta Part A Mol. Spectrosc.*, vol. 24, no. 8, pp. 965–968, 1968, doi: 10.1016/0584-8539(68)80115-1.

[70] M. Dieterle, G. Weinberg, and G. Mestl, "Raman spectroscopy of molybdenum oxides - Part I. Structural characterization of oxygen defects in MoO3-x by DR UV/VIS, Raman spectroscopy and X-ray diffraction," *Phys. Chem. Chem. Phys.*, vol. 4, no. 5, pp. 812–821, 2002, doi: 10.1039/b107012f.

[71] R. L. Frost and M. Weier, "Raman microscopy of selected autunite minerals," *Neues Jahrb. fur Mineral. Monatshefte*, vol. 5, no. 12, pp. 575–594, 2004, doi: 10.1127/0028-3649/2004/2004-0575.

[72] M. Dieterle and G. Mestl, "Raman spectroscopy of molybdenum oxides: Part II. Resonance Raman spectroscopic characterization of the molybdenum oxides Mo4O11 and MoO2," *Phys. Chem. Chem. Phys.*, vol. 4, no. 5, pp. 822–826, 2002, doi: 10.1039/b107046k.